




Ultrafast spin wave propagation in thick magnetic insulator films with perpendicular magnetic anisotropy

Yiheng Rao ^{1,2,*}, Qinghui Yang,^{3,*} Qi Wang ⁴, Guokun Ma,^{1,2} and Jie Li ³

¹*School of Microelectronics, Hubei University, Wuhan 430062, People's Republic of China*

²*Hubei Yangtze Memory Laboratories, Wuhan 430205, People's Republic of China*

³*State Key Laboratory of Electronic Thin Films and Integrated Device, University of Electronic Science and Technology of China, Chengdu 611731, People's Republic of China*

⁴*Faculty of Physics, University of Vienna, Boltzmannngasse 5, A-1090 Vienna, Austria*



(Received 14 July 2021; revised 29 October 2021; accepted 30 November 2021; published 17 December 2021)

Magnetostatic forward volume spin-waves (MFVSWs) are magnetic moments propagated perpendicular to the film plane and offer reciprocity configurations, which is suitable for spin-wave logic devices with low power consumption. However, owing to the strong shape anisotropy field, magnetic films are easily magnetized in the film plane. Fabrication of thick magnetic films with low Gilbert damping and large perpendicular magnetization anisotropy was an unsolved problem. The promising materials with low damping and easy to modify properties are $Y_3Fe_5O_{12}$ -based single-crystal films. High quality $(Y_{1.26}Bi_{0.18}Lu_{0.96}Ca_{0.6})(Fe_{4.4}Ge_{0.6})O_{12}$ micrometer-thick films with strong anisotropy field up to 1862 Oe, narrow out-of-plane ferromagnetic resonance linewidth as low as 2 Oe, and low Gilbert damping approximately $(7.06 \pm 0.15) \times 10^{-5}$ grow on the gadolinium gallium garnet substrate successfully. The garnet film shows a MFVSW group velocity of 2.25 km/s, relaxation time 50 ns, and decay length up to 115 μm , paving the road towards ultralow power dissipation magnonic devices (microwave devices) based on magnetic insulators.

DOI: [10.1103/PhysRevB.104.224422](https://doi.org/10.1103/PhysRevB.104.224422)

I. INTRODUCTION

Spin waves (SWs) and their quanta magnons provide a promising way to transport information with low power consumption. They are reconfigurable by forming magnon crystals [1–3], periodic optical structures [4], applying voltage [5,6], and so on [7]. In practical devices, SWs should propagate over long distances through thin films. In this case, the most studied and promising material is yttrium iron garnet (YIG) [8,9], which has a low damping constant (long SW decay length) and insulation characteristics (no charge current). Damon-Eshbach SW (DESW) modes were most studied, which require a magnetic bias field in the film plane [10,11]. Unfortunately, DESWs are nonreciprocal, causing the signal waveguide to be patterned only in one direction; any bends in a structure can cause significant energy loss. Forward volume magnetostatic spin waves (MFVSWs) have intrinsic advantages, such as strong SW excitation strength and reciprocity transmission properties [12,13]. Relatively high magnetic fields are acceptable but require large magnetic systems for the film biasing [11]. The use of magnetic films with a large perpendicular magnetic anisotropy (PMA) will reduce the size and weight of the magnetic system. Therefore, the development of low-damping magnetic materials with a large PMA is essential for the practical applications of magnonic devices. Such materials are needed in spin

Hall nano-oscillators [14,15], spin-wave logic gates [16,17], spin-wave couplers [18,19], spin-wave filters [20], and phase conjugate mirrors [21].

Ferrimagnetic metals with PMA are studied in several works [22–24]. Ultrathin metal film or metal/Pt structures can induce PMA in magnetic layers. The problem lies in the broad ferromagnetic resonance (FMR) linewidth. Therefore, some researchers tried to introduce anisotropy in a low-damping ferrimagnetic insulator, YIG. The most common method is replacing the gadolinium gallium garnet (GGG) substrate with another garnet substrate with a giant crystal lattice [25]. This method can slightly pull the magnetic moments out of the plane and enhance the damping constant enormously. YIG film properties can be modified using rich doping combinations or other iron garnets, increasing growth-induced anisotropy, stress-induced anisotropy, or magnetocrystalline anisotropy [26–30]. However, the FMR linewidth and high damping cause a relatively small decay length [31]. Increasing the film thickness is an efficient way to decrease damping and increase group velocity. However, the strain relaxation limits the thickness to tens of nanometer even with a top layer [32].

Therefore, in this study, we analyzed the dynamic properties of a garnet material $(Y_{1.26}Bi_{0.18}Lu_{0.96}Ca_{0.6})(Fe_{4.4}Ge_{0.6})O_{12}$ (YBLCIG) on GGG substrate. The film maintains PMA with a film thickness of up to 1 μm without significant stress relaxation. Several ions replace Y^{3+} at dodecahedral sites and Fe^{3+} at tetrahedral sites in our approach. The doping enabled us to modify the saturation magnetization ($4\pi M_s$) and interface stress of the garnet film. A fine GGG/YBLCIG structure with a large PMA was obtained with

*Corresponding authors: yihengrao@163.com; yangqinghui@uestc.edu.cn

careful control of the growth temperature. Utilizing the film as the SW waveguide, MFVSWs are excited with a magnetic field ten times smaller than traditional single-crystal stress-free YIG with micrometer thickness. We also determine the group velocity, the decay length, and relaxation time of the film.

II. EXPERIMENT AND RESULTS

A. Material design and fabrication

Recent studies on SWs for small-size device fabrication are mainly based on thin films with thickness in nanometer rather than micrometer scale. However, the flat dispersion relation in the dipolar region for ultrathin films leads to low SW group velocity [33]. The damping parameter is also dependent on the thickness of garnet films [34]. Stress-modified PMA materials can maintain anisotropy only in films with low thickness [25,29,30,35]. A low damping thick garnet film with PMA based on YIG has been designed and fabricated by liquid phase epitaxy (LPE). The composition of this garnet is $(Y_{1.26}Bi_{0.18}Lu_{0.96}Ca_{0.6})(Fe_{4.4}Ge_{0.6})O_{12}$. Bi^{3+} ions increase the magnetocrystalline anisotropy [36], and Lu^{3+} ions adjust the lattice constant to match with that of GGG [37] since the Lu^{3+} has a radius 0.97 Å smaller than the radius Bi^{3+} (1.11 Å) and Ca^{2+} (1.12 Å); Ge^{4+} ions partially replaced Fe^{3+} ions for reducing the $4\pi M_s$ of the material. Ca^{2+} ions at the dodecahedral site maintain the charge balance of the system.

The YBLCIG films were grown on 3-in. GGG (111) substrates using the vertical dipping LPE technique. LPE is the best method for garnet film fabrication. The GGG substrates were cleaned in hot potassium dichromate solution for 3 s and then in $NaOH + Na_2CO_3$ aqueous alkaline isopropanol for 3 min before being moved into dilute ammonia water. After that, organic distillation was used to further clean the surface of the substrate before transferring it into the vertical growth chamber connected to the atmosphere. The GGG substrate fixed on a Pt holder was dipped into the 801 °C melt in a Pt crucible with a descent rate of 60 mm/min and a rotation rate of 60 r/s. On removing the substrate from the melt after 4 min of growth, a double-sided film was obtained. We kept the substrate above the melt for 30 min and lifted it out from the chamber at a speed of 60 mm/min, corresponding to an annealing procedure of about 15 min. The residue present on the film was cleaned in boiling acetic acid for 20 min after removing it from the growth chamber.

The crystal quality, interface structure, and energy dispersive spectrometer (EDS) profiles were studied using high-resolution scanning transmission electron microscopy (FEI Talos F200) of a GGG/YBLCIG sample cross section. The material crystal quality is characterized by x-ray diffraction (XRD) using Jordan Valley's D1 Evolution with a filter of $Cu-K\alpha$, $k = 1.5406$ Å, radiation in the reflection mode.

B. VNA-FMR and SW spectroscopy

Vector network analyzer-FMR (VNA-FMR) is an efficient method to analyze the dynamic properties of ferromagnetic materials. This method is executed using a two-port VNA (R&S ZNB40) and a self-made microwave rotatable probing station with a bipolar electromagnet. FMR spectra were

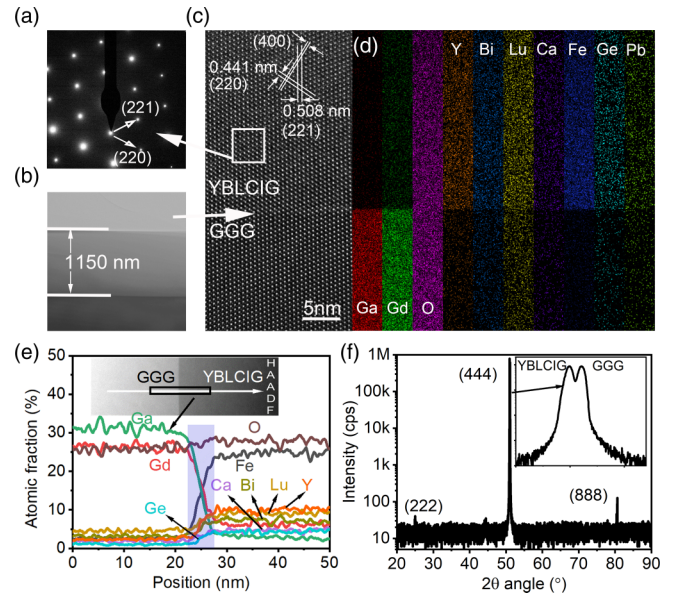


FIG. 1. STEM characterization of the YBLCIG/GGG structure. (a) Selected-area diffraction image, (b) confirmation of film thickness using the topography image, (c) high-resolution image of YBLCIG/GGG interface, (d),(e) plane and line scanning analysis of EDS for the elemental distribution at the interface, (f) XRD ω - 2θ scan of YBLCIG film grown on GGG (111) substrate, with the enlarged curve in the inset showing the (444) peak.

recorded for various in-plane (IP) and out-of-plane (OOP) external magnetic bias fields by measuring the S_{21} scattering parameter on the YBLCIG film with a coplanar waveguide (CPW) patterned on it. The signal line and the ground line of this CPW had widths of 80 and 200 μm , respectively, and were separated by a gap of 40 μm . The VNA provided microwave current with a power of about -10 dBm through a ground-signal-ground (GSG) probe used to generate a radio frequency (rf) magnetic field around the CPW. Another GSG probe detects the transmission energy through the CPW. The CPW was fabricated by photolithography and consisted of 10 nm Ta and 100 nm Au. Both metals were deposited by magnetron sputtering.

Similar to the VNA-FMR setups, electrical characterization techniques were used to detect and excite SWs, but with two antennas for obtaining the parameters mentioned above. The VNA was connected to the antennas using microwave cables and GSG probes. S parameters were extracted from the S_{12} transmission spectra from the VNA with an external H applied perpendicular to the film plane. The VNA offers -10 dBm excitation power of the microwave signal to avoid nonlinear excitations in the film.

C. Film structure characterization

An 1150-nm-thick film is chosen for this work, and Fig. 1(b) shows the cross-section image. The high-resolution image of the interface between the YBLCIG film and the GGG substrate is shown in Fig. 1(c). No evidence of dislocations was found in the YBLCIG crystal structure at the interface over the field of the images. Crystal faces of (221),

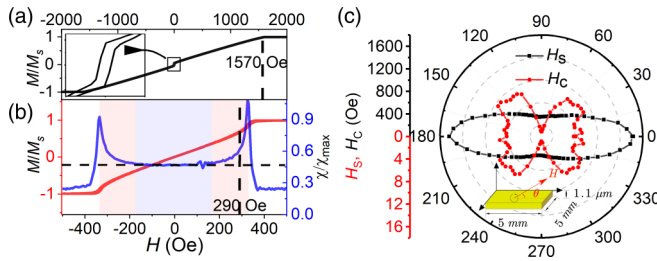


FIG. 2. Static magnetic properties of the studied film. (a),(b) Normalized IP and OOP VSM loops of the studied film; the blue curve is a branch of the normalized magnetic susceptibility of OOP VSM loop, (c) azimuthal angle dependencies of H_s , and H_c of the sample film with dimensions of $5 \text{ mm} \times 5 \text{ mm} \times 1.1 \text{ }\mu\text{m}$.

(220), (400) are confirmed and labeled in the figure according to the power diffraction file of YIG. The interplanar crystal spacings are calculated by the diffraction pattern of the area marked by the white rectangle shown in Fig. 1(a). The (221) and (220) crystal faces have interplanar crystal spacings of 5.08 and 4.41 Å, respectively. The parallelogram diffraction pattern indicates the formation of a well-structured single-crystal film. As a cubic crystal, the lattice parameter of the garnet film is about 12.423 Å, determined by interplanar crystal spacing and indices of the crystal face. The energy dispersive spectrometer (EDS) of the plane and the line scans [Figs. 1(d) and 1(e)] indicates limited interdiffusion of the cations at the interface. A few Pb ions are present as impurities in the film coming from the solvent. The blue block in Fig. 1(e) indicates a 5-nm transition layer at the interface. Figure 1(f) shows the x-ray diffraction spectrum of the studied film. The (222), (444), (888) diffraction peaks of the film are observed. The enlarged (444) peak is shown in the inset. The GGG and YBLGIG peaks are overlapped, indicating a fine match between the substrate and the film. The narrow linewidth and significant signal intensity indicate the formation of a well-crystallized film.

D. Static and dynamic magnetic characterization

The static magnetic properties of the films have been characterized using vibrating sample magnetometry (Lake Shore 8604 VSM) and scanning laser magneto-optical Kerr effect (MOKE) magnetometer (Durham Magneto-Optics Ltd NanoMOKE 3). The normalized IP and OOP VSM curves were acquired by removing the substrate signal from the original signal [see Supplemental Material Fig. S1(a) [38]] shown in Figs. 2(a) and 2(b). The $4\pi M_s$ value is approximately 702.4 G for the film, and the inset of Fig. 2(a) shows the in-plane easy magnetization phase. The blue curve in Fig. 2(b) is the normalized magnetic susceptibility obtained by differentiating the $\varphi = 90^\circ$ VSM loop, and only one branch is shown (-2000 – 2000 Oe). The previous studies [39] present clear images of the domain growth in a perpendicular recording medium varying with H . The first part is the reversible domain wall displacement indicated in the blue block with linear magnetization. The following process is the rotation of the domain moments, a rapid magnetization process leading to a nearly single domain state. For this film, this process was reversible, ending at approximately 290 Oe. This value was

determined based on the switch-on magnetic field of the SW in the last section. The last part is the rotation of an in-plane easy magnetization phase, pinned magnetic moments, and magnetic bubbles; this is an intense and irreversible process leading to the most rapid increase in magnetization with the reversal of the magnetic moments. The saturation field for OOP magnetization H_s^\perp is 337.8 Oe, and IP magnetization H_s^\parallel is 1607.4 Oe. The OOP Kerr loop has a shape similar to the VSM curve with a saturation field of 356.1 Oe in Fig. S1(b) of the Supplemental Material [38]. The Bi^{3+} doping has the effect of enhancing the magneto-optical response [40,41]. The Kerr rotation coefficient reaching up to $\theta = 436.1 \text{ mdeg}/\mu\text{m}$ using a 660-nm laser for a saturated film in Fig. S1(b). This value is comparable with magneto-optical materials such as TmBiIG ($0.5^\circ/\mu\text{m}$) and LuBiIG ($2^\circ/\mu\text{m}$) [42]. For optical-based SW measurements [43–45], a sizeable magneto-optical effect is needed to increase the measurement system's sensitivity.

Azimuthal angle dependencies for the VSM loop parameters of the studied sample were characteristic and appeared in the polar plots versus the angle φ shown in Fig. 2(c). The azimuthal dependence of the saturation field H_s revealed the twofold symmetry, indicating a strong OOP anisotropy as expected. The easy axis and hard axis are at $\varphi = 90^\circ$ (270°) and 0° (180°). The obtained H_c polar plot shows an interesting twofold butterflylike loop. $\varphi = 90^\circ$ and 270° respectively, representing the head and tail, have the smallest H_c value of 0.8 Oe. H_c increased rapidly to 8.5 Oe forming the two “wings” with the applied field deviating from the easy axis. In the angle ranges of -20 – 20° or 160 – 200° , the H_c value decreased to approximately 6.2 Oe. The decrease of H_c from 8.5 to 6.2 Oe was caused by the existence of the easy magnetization phase present in the $\varphi = 0^\circ$ curve in Fig. 2(a). In Fig. S1(c), the polarization microscopy observes the magnetic domain structures of YBLGIG films after demagnetization; the μm -wide mazelike magnetic domains demonstrate that the easy magnetic axis is perpendicular to the film surface [29].

The most significant feature of the film is its low magnetic loss that can be characterized via the VNA-FMR method. The IP-FMR measurements were carried out in the 4–13-GHz range. The OOP-FMR measurements were carried in the 4–9-GHz range. Figure 3(a) shows the field-frequency signal maps in the range 0–800 Oe and 4–5.5 GHz obtained from OOP-FMR measurements. The saturated OOP-FMR spectra can only be detected with H above 330.7 Oe. The FMR spectra at 0–330.7 Oe show the film's domain resonance at unsaturated magnetization states. The resonance properties depend strongly on the behavior of static magnetization. The behavior of resonance frequency as a function of H is determined by the $H-4\pi M$ value derived from the OOP-VSM measurement shown in Fig. 3(a) (white dash line). Figure 3(b) gives the resonance spectra and linewidth at the multidomain state. Domain growth leading to an increased power absorption at the magnetic field ranges 0–178.1 Oe. On the contrary, the decrease of internal field H_0 restrains power absorption and is a dominant factor in field range 178.1–333.8 Oe. The minimum FMR linewidth and largest power absorption for domain resonance (Δf_{domain}) is 18.9 MHz at the H of 178.1 Oe, with resonance frequency up to 4.8 GHz. The resonance frequency f_{FMR} as a function of H for both FMR configurations (IP and

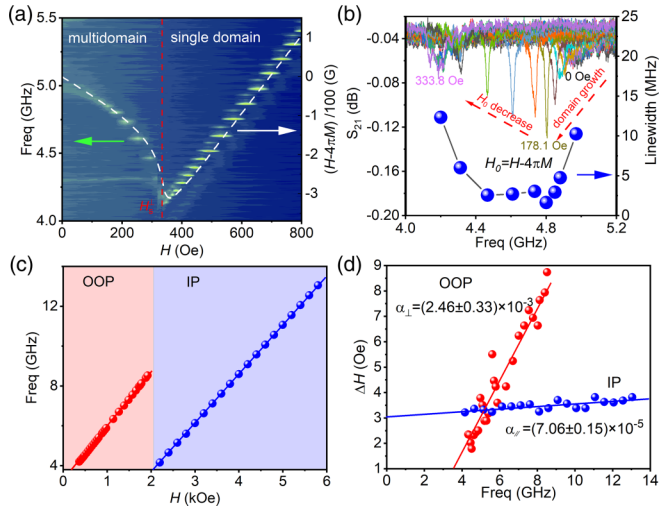


FIG. 3. Dynamic magnetic properties of the film with PMA. (a) Field frequency of FMR signal map for the film at the multidomain state and single domain state; the white dash line is the internal field $H_0 = H - 4\pi M$ versus H without considering anisotropy field. (b) Domain resonance behavior versus H at multidomain state. (c) Resonance frequency of the main mode as a function of H for OOP (red block) and IP (blue block) FMR configuration. (d) Frequency dependence of the FMR linewidth. The calculated Gilbert damping parameter and the extrinsic linewidth are displayed on the graph.

OOP) is shown in Fig. 3(c). Using the IP frequency dependence of FMR, we derived the effective magnetization (M_{eff}) using the Kittel law [29]:

$$f_{\text{FMR}}^{\parallel} = \gamma_{\parallel} \sqrt{H(H + 4\pi M_{\text{eff}})},$$

where γ_{\parallel} is the gyromagnetic ratio fitted using the IP-FMR H - f_{FMR} plot. The fitted γ_{\parallel} value is 2.72 ± 0.06 MHz/Oe, and the $4\pi M_{\text{eff}}$ value is -1162 G. The uniaxial magnetic anisotropy field H_a can be derived using the saturation magnetization from VSM magnetometry as follows $4\pi M_{\text{eff}} = 4\pi M_s - H_a$. We obtained the H_a value of approximately 1862 Oe, which is large enough to compensate the film entirely. To further verify the fitting result, the experimental data of FMR measurements with the external magnetic field applied with an OOP orientation were fitted with the following equation [30]:

$$f_{\text{FMR}}^{\perp} = \gamma_{\perp} (H + H_a - 4\pi M_s).$$

The fitted anisotropy field was 1819 Oe, which is in agreement with the IP-FMR result. The fitted γ_{\perp} value was 2.86 ± 0.08 MHz/Oe, which is slightly larger than γ_{\parallel} , but within acceptable limits.

Other important parameters of this material are the FMR linewidth and damping. We extracted the full width at half maximum (FWHM) of the main Δf versus resonance peaks using a Lorentzian function and converted the Δf to magnetic field scale ΔH shown in Fig. 3(d) [46]. The lines in Fig. 3(d) are the fitted Gilbert damping constant using the formula [10] $\Delta H = 2\alpha f/\gamma + \Delta H_0$. The IP damping parameter $\alpha_{\parallel} = (7.06 \pm 0.15) \times 10^{-5}$ is considerably small and comparable with that for YIG films. However, Δf is around three times

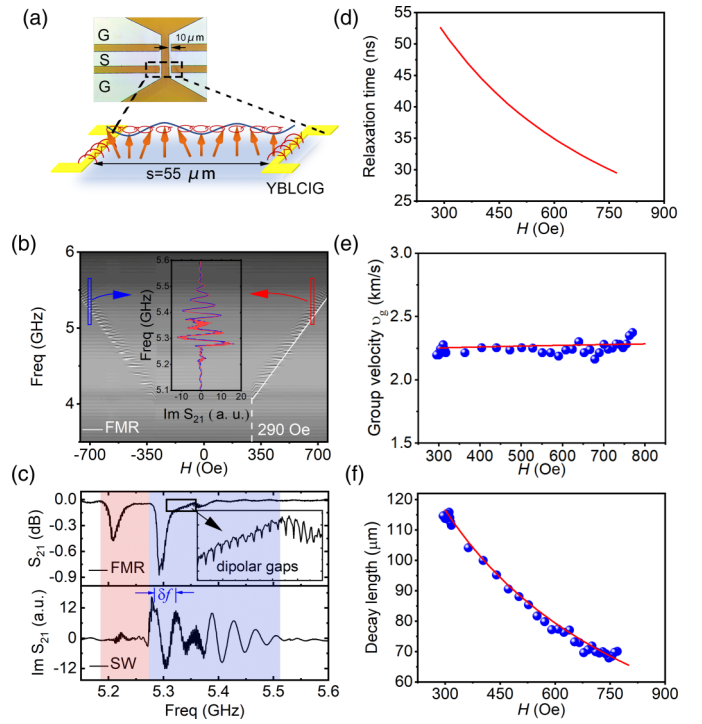


FIG. 4. Spin-wave transmission in YBLCIG film with strong PMA. (a) Simulated spin-wave excitation spectrum of the antenna with $10\text{-}\mu\text{m}$ signal linewidth. (b) Color-coded measured and expected spin-wave intensities as a function of the applied frequency and H ; the inset figure is the imaginary part of S_{21} for 715 and -714.7 Oe. (c) Comparisons of FMR and SW at the same H . Panels (d)–(f) represent the measured (dots) and calculated (lines) relaxation time, group velocity, and decay length as a function of H , respectively.

larger than pure YIG [34] because of the increasing inhomogeneous linewidth caused by doping. The OOP damping parameter $\alpha_{\perp} = (2.46 \pm 0.33) \times 10^{-3}$ is more than one order higher than the IP damping parameter due to several reasons, such as two-magnon scattering [47], magnetization pinning [48], and inhomogeneities of the sample [49]. Recently, a similar angular-dependence behavior has been reported [29]. Despite this, the damping is still the most minor reported OOP damping value.

E. Propagating forward volume magnetostatic spin waves

Based on the magnetic properties discussed above, a film with large PMA and low damping is obtained using LPE with ion doping. The propagation of MFVSW in the present film is investigated and discussed from a practical viewpoint. The main parameters studied were the f - H relation, reciprocity, group velocity, relaxation time, and decay length. The colored inset of Fig. 4(a) shows the sketch of the investigated device and the optical photograph of the patterned antennas on the studied film. The $10\text{-}\mu\text{m}$ -wide antenna mainly excited SWs with wave vectors k ranging $0\text{--}0.75$ rad/ μm , shown in Supplemental Material Fig. S3 [38,50].

Color-coded measured and expected SW intensities (the imaginary part of the S_{21} spectrum) as a function of the applied frequency and H with an input microwave power of 0

TABLE I. Key parameters reported for magnetic films with PMA.

Material ^d	t (nm)	M_s	H_u (Oe)	H_s^{op} (Oe)	$\Delta H_{//}$	ΔH_{\perp}	α^b (10^{-3})	H_{res}^c (GHz/Oe)	l_d (μm)	v_g (km/s)
G/YBLCIG (this study)	1150	702 Oe	1862	337.8	3.2 Oe/ 8.6 MHz	2 Oe/ 5 MHz	2.46 $_{\perp}$ / 0.07 $_{//}$	4.2/340 $_{\perp}$	115	2.25
G/Mn:YIG [30]	≤ 30	125 kA/m	2100	50	90 MHz		8 $_{//}$	4/900 $_{\perp}$	3.7	0.15
S/SmG/YIG [32]	≤ 20	1614–1718 Oe	–432	≈ 50				9.1/3000 $_{\perp}$		
S/SmG/YIG/SmG [32]	≤ 40	1689 \pm 28 Oe	–300	≈ 50				9.1/2800 $_{\perp}$		
S/YBiLuFeAlIG [54]	500	43.8 emu/cm	850				2			
S/YBiIG [29]	8–50	1800 Oe	3310	10	150 Oe ^a	950 Oe ^a	1.9 $_{//}$			
G/EuIG [55]	56	110 emu/cm	1370	500			24.2 $_{\perp}$	6/4500 $_{\perp}$		
S/TmIG [56]	10	1393 Oe	3393	≈ 100	167 Oe	224 Oe		9.3/1900 $_{\perp}$		
Ni/Co-virgin [57]	≤ 1	475 kA/m			≈ 900	≈ 200 Oe	44 $_{\perp}$	10/1000 $_{\perp}$		
Ni/Co-irradiated [57]	≤ 1	475 kA/m			≈ 500	≈ 350 Oe	39 $_{\perp}$	10/5000 $_{\perp}$		
Ta/Al/CoFe/Al/Ta [58]	1.8	2.35 T	–600			90 Oe		10/15 000 $_{\perp}$		
W/CoFeB/MgO/Ta [59]	1.2	780 emu/cm					15–200 $_{\perp}$	20/10 000 $_{//}$		

^aPeak-to-peak value ΔH_{pp} of the derivative of FMR absorption transformed into $\Delta H = \sqrt{3}\Delta H_{pp}$.

^bsome works give only the in-plane damping parameter.

^cthe resonant frequency at a specific magnetic field.

^dthe capital letter G represents GGG; the S represents SGGG.

dBm are shown in Fig. 4(b). One can see that the SW spectra cannot be detected below 290 Oe without significant signal attenuation. In VSM measurements, we obtained the OOP H_s value 337.8 Oe, which is slightly higher than 290 Oe. Based on the analysis of technical magnetization, the multidomain state (under an H of ~ 290 Oe) blocked the SW propagation path in our experimental setup [31]. However, the SW forbidden gap may become a potential region for domain or domain wall SW propagation channels on carefully controlling the direction of the domain stripes [51]. The inset of Fig. 4(b) shows the comparison of the MFVSW signals of the S_{12} transmission spectra at -715.8 and 714.7 Oe. One can observe that the frequencies and amplitudes show almost no discrepancies, indicating that the MFVSWs do not have a nonreciprocity effect. This property solves the problem of heavy losses in SW guides with bends in their structures. Figure 4(c) presents the OOP-FMR spectra with an H of approximately 713.6 Oe and the SW signals of the S_{12} transmission spectra at 714.7 Oe. The two resonance peaks correspond to two SW modes as the red and blue areas indicate. The two SW modes seem to have no apparent interactions with each other. The full FMR spectra and part of the SW spectra have comblike oscillation peaks with peak separation at approximately 3.35 MHz. These peaks originate from magnetoacoustic interaction between spin waves propagating in the YBLCIG film and Lamb modes of acoustic waves in GGG substrate [52,53].

The following discussion is based on the primary SW mode shown in the blue block of Fig. 4(c). To calculate the relaxation time τ , group velocity v_g , and decay length l_d , the dispersion equation for the dipolar spin wave at forward volume mode is simplified as follows:

$$\omega = \sqrt{\omega_H \{ \omega_H + \omega_M [1 - (1 - e^{-kd}) / (kd)] \}},$$

where $\omega_H = \gamma H_{int} = \gamma(H + H_a - 4\pi M_s)$, $\omega_M = \gamma 4\pi M_s$.

We extracted the group velocity from experiment results using the following equation [31]:

$$v_g = \frac{\partial \omega}{\partial k} \approx \frac{2\pi \delta f}{2\pi/s} = \delta f s,$$

and calculated the group velocity by

$$v_g = \frac{\partial \omega}{\partial k} = \frac{-\omega_H \omega_M (dke^{-dk} - 1 + e^{-dk})}{2\omega dk^2},$$

where $s = 55 \mu\text{m}$ is the distance between two antennas in our experiments; δf is the frequency separation of two neighboring maxima indicating the phase shift of 2π shown in Fig. 4(c). The extracted (blue dots) and calculated v_g (red line) versus the H curve is shown in Fig. 4(e). Note that the MFVSW spin-wave group velocity is weakly dependent on the external magnetic field and has a value of about 2.25 km/s. The relaxation time τ is estimated [52] to be

$$\begin{aligned} \tau &= \left(-\frac{\gamma \Delta H}{2\omega} \omega \frac{\partial \omega}{\partial \omega_H} \right)^{-1} \\ &= \left[-\frac{\gamma \Delta H}{2\omega} \left(\omega_H + \frac{\omega_M}{2} [1 - (1 - e^{-kd}) / (kd)] \right) \right]^{-1}. \end{aligned}$$

τ versus H shown in Fig. 4(d) is determined via the OOP-FMR results in Fig. 3(d). The SW decay length in Fig. 4(f) was derived using the relation $l_d = v_g \times \tau$, using the experimental and calculated curves in Figs. 4(d) and 4(e) as inputs. The estimated MFVSW decay length was up to 115 μm at $H \approx 300$ Oe. The decay length decreases with the increase of the magnetic bias field to approximately 70 μm at $H \approx 770$ Oe. A considerable decay length like this is essential for the implementation of SW-based devices.

From previous reports about magnetic films with PMA, available geometry, static, and dynamic parameters were taken and summarized in Table I. The reported film thickness ranges from less than 1 nm to 50 nm, much thinner than the studied one. The PMA enhances the FMR linewidth obviously, up to

tens of hundreds of Oersted. The Gilbert damping coefficient α was found in the range 1.0×10^{-3} –0.2. The lowest damping was also obtained from YIG-based films. Due to large dynamic loss, most PMA films unable to support SWs propagate over a detectable distance. The studied film shows outstanding decay length and group velocity.

III. CONCLUSION

In summary, we described a thick garnet film with ultralow damping and fast spin-wave group velocity epitaxial on a (111) GGG substrate via LPE. Doping with Bi^{3+} , Lu^{3+} , Ca^{2+} , and Ge^{4+} led to PMA of the garnet film even at film thickness up to $1 \mu\text{m}$. Films also show ultralow damping in both OOP (2.46 ± 0.33) $\times 10^{-3}$ and IP (7.06 ± 0.15) $\times 10^{-5}$. From a practical point of view, a low magnetic bias field, ten times smaller than that in YIG, is needed to meet the propagation conditions of MFVSWs. To the best of our knowledge, the group velocity, relaxation time, and decay length are superior to other reported PMA materials. Because of Bi^{3+} doping, the

magneto-optical properties can help study the interactions of magnons and phonons in garnet. Low damping, PMA, and a large Kerr rotation angle make this material a promising candidate for magnonic, spintronic, and magneto-optical device applications. Besides, the small FMR linewidth for domain resonance makes the film functional at a small H with high frequency. Based on this film and its properties, the applicable non-magnetic-field spin wave device can be expected.

ACKNOWLEDGMENTS

This work was supported by the International Cooperation Project under Grant No. SQ2018YFE0205600, Hubei Key Laboratory of Advanced Memories, Scientific Research Project of Education Department of Hubei Province (Grant No. Q20211002), National Key Scientific Instrument and Equipment Development Project No. 51827802, the National Natural Science Foundation of China (Grants No. 51702042, No. 61734002, No. 51872041, and No. 61571079), and the International Science & Technology Cooperation Program of China (Grant No. 2015DFR50870).

-
- [1] A. Haldar, D. Kumar, and A. O. Adeyeye, *Nat. Nanotechnol.* **11**, 437 (2016).
- [2] K. S. Lee, D. S. Han, and S. K. Kim, *Phys. Rev. Lett.* **102**, 127202 (2009).
- [3] S. Tacchi, G. Duerr, J. W. Klos, M. Madami, S. Neusser, G. Gubbiotti, G. Carlotti, M. Krawczyk, and D. Grundler, *Phys. Rev. Lett.* **109**, 137202 (2012).
- [4] M. Vogel, A. V. Chumak, E. H. Waller, T. Langner, V. I. Vasyuchka, B. Hillebrands, and G. von Freymann, *Nat. Phys.* **11**, 487 (2015).
- [5] B. Rana and Y. C. Otani, *Phys. Rev. Appl.* **9**, 014033 (2018).
- [6] Q. Wang, A. V. Chumak, L. Jin, H. Zhang, B. Hillebrands, and Z. Zhong, *Phys. Rev. B* **95**, 134433 (2017).
- [7] D. Grundler, *Nat. Phys.* **11**, 438 (2015).
- [8] H. Qin, G. J. Both, S. J. Hamalainen, L. Yao, and S. van Dijken, *Nat. Commun.* **9**, 5445 (2018).
- [9] A. A. Serga, A. V. Chumak, and B. Hillebrands, *J. Phys. D: Appl. Phys.* **43**, 264002 (2010).
- [10] H. Qin, S. J. Hämäläinen, K. Arjas, J. Witteveen, and S. van Dijken, *Phys. Rev. B* **98**, 224422 (2018).
- [11] J. Chen, C. Liu, T. Liu, Y. Xiao, K. Xia, G. E. W. Bauer, M. Wu, and H. Yu, *Phys. Rev. Lett.* **120**, 217202 (2018).
- [12] J. Chen, F. Heimbach, T. Liu, H. Yu, C. Liu, H. Chang, T. Stückler, J. Hu, L. Zeng, Y. Zhang, Z. Liao, D. Yu, W. Zhao, and M. Wu, *J. Magn. Magn. Mater.* **450**, 3 (2018).
- [13] K. Shimada, T. Goto, N. Kanazawa, H. Takagi, Y. Nakamura, H. Uchida, and M. Inoue, *J. Phys. D: Appl. Phys.* **50**, 275001 (2017).
- [14] M. Collet, X. de Milly, O. d'Allivy Kelly, V. V. Naletov, R. Bernard, P. Bortolotti, J. Ben Youssef, V. E. Demidov, S. O. Demokritov, J. L. Prieto, M. Munoz, V. Cros, A. Anane, G. de Loubens, and O. Klein, *Nat. Commun.* **7**, 10377 (2016).
- [15] R. H. Liu, W. L. Lim, and S. Urazhdin, *Phys. Rev. Lett.* **114**, 137201 (2015).
- [16] N. Kanazawa, T. Goto, K. Sekiguchi, A. B. Granovsky, C. A. Ross, H. Takagi, Y. Nakamura, H. Uchida, and M. Inoue, *Sci. Rep.* **7**, 7898 (2017).
- [17] A. B. Ustinov, E. Lahderanta, M. Inoue, and B. A. Kalinikos, *IEEE Magn. Lett.* **10**, 1 (2019).
- [18] Q. Wang, P. Pirro, R. Verba, A. Slavin, B. Hillebrands, and A. V. Chumak, *Sci. Adv.* **4**, 1701517 (2018).
- [19] Q. Wang, M. Kewenig, M. Schneider, R. Verba, F. Kohl, B. Heinz, M. Geilen, M. Mohseni, B. Lägel, F. Ciubotaru, C. Adelman, C. Dubs, S. D. Cotozana, O. V. Dobrovolskiy, T. Brächer, P. Pirro, and A. V. Chumak, *Nat. Electron.* **3**, 765 (2020).
- [20] X. Yang, J. Wu, S. Beguhn, T. Nan, Y. Gao, Z. Zhou, and N. X. Sun, *IEEE Microwave Wireless Compon. Lett.* **23**, 184 (2013).
- [21] A. Inglis, C. J. Tock, and J. F. Gregg, *SN Appl. Sci.* **1**, 480 (2019).
- [22] H. Yang, A. D. Vu, A. Hallal, N. Rougemaille, J. Coraux, G. Chen, A. K. Schmid, and M. Chshiev, *Nano Lett.* **16**, 145 (2016).
- [23] C. Hin Sim, J. Cheng Huang, M. Tran, and K. Eason, *Appl. Phys. Lett.* **104**, 012408 (2014).
- [24] A. Haldar, C. Tian, and A. O. Adeyeye, *Sci. Adv.* **3**, e1700638 (2017).
- [25] H. Wang, C. Du, P. C. Hammel, and F. Yang, *Phys. Rev. B* **89**, 134404 (2014).
- [26] C. Tang, P. Sellappan, Y. Liu, Y. Xu, J. E. Garay, and J. Shi, *Phys. Rev. B* **94**, 140403(R) (2016).
- [27] C. O. Avci, A. Quindeau, C. F. Pai, M. Mann, L. Caretta, A. S. Tang, M. C. Onbasli, C. A. Ross, and G. S. Beach, *Nat. Mater.* **16**, 309 (2017).
- [28] A. Quindeau, C. O. Avci, W. Q. Liu, C. L. Sun, M. Mann, A. S. Tang, M. C. Onbasli, D. Bono, P. M. Voyles, Y. B. Xu, J. Robinson, G. S. D. Beach, and C. A. Ross, *Adv. Electron. Mater.* **3**, 1600376 (2017).

- [29] L. Soumah, N. Beaulieu, L. Qassym, C. Carretero, E. Jacquet, R. Lebourgeois, J. Ben Youssef, P. Bortolotti, V. Cros, and A. Anane, *Nat. Commun.* **9**, 3355 (2018).
- [30] C. T. Wang, X. F. Liang, Y. Zhang, X. Liang, Y. P. Zhu, J. Qin, Y. Gao, B. Peng, N. X. Sun, and L. Bi, *Phys. Rev. B* **96**, 224403 (2017).
- [31] J. Chen, C. Wang, C. Liu, S. Tu, L. Bi, and H. Yu, *Appl. Phys. Lett.* **114**, 212401 (2019).
- [32] J. Fu, M. Hua, X. Wen, M. Xue, S. Ding, M. Wang, P. Yu, S. Liu, J. Han, C. Wang, H. Du, Y. Yang, and J. Yang, *Appl. Phys. Lett.* **110**, 202403 (2017).
- [33] S. Maendl, I. Stasinopoulos, and D. Grundler, *Appl. Phys. Lett.* **111**, 012403 (2017).
- [34] C. Dubs, O. Surzhenko, R. Linke, A. Danilewsky, U. Bruckner, and J. Dellith, *J. Phys. D: Appl. Phys.* **50**, 204005 (2017).
- [35] Y. H. Rao, D. N. Zhang, H. W. Zhang, L. C. Jin, Q. H. Yang, Z. Y. Zhong, M. M. Li, C. Y. Hong, and B. Ma, *J. Phys. D: Appl. Phys.* **51**, 435001 (2018).
- [36] J. Mada and K. Yamaguchi, *J. Appl. Phys.* **57**, 3882 (1985).
- [37] K. Iida, N. Kawamae, S. Hoshi, T. Machi, T. Kono, J. Yoshioka-Kato, N. Chikumoto, N. Koshizuka, N. Adachi, and T. Okuda, *Jpn. J. Appl. Phys.* **44**, 1734 (2005).
- [38] See Supplemental Material at <http://link.aps.org/supplemental/10.1103/PhysRevB.104.224422> for VSM and MOKE spectral analyses of YBLCIG films, the domain structure of the sample, the angle dependence of FMR analysis of the YBLCIG film, and SW excitation spectrum of the used antenna.
- [39] A. Hubert and R. Schäfer, *Magnetic Domains* (Springer, New York, 1998).
- [40] F. Hansteen, L. Egil Helseth, T. H. Johansen, O. Hunderi, A. Kirilyuk, and T. Rasing, *Thin Solid Films* **455-456**, 429 (2004).
- [41] K. Matsumoto, S. Sasaki, K. i. Haraga, K. Yamaguchi, T. Fujii, and Y. Asahara, *J. Appl. Phys.* **71**, 2467 (1992).
- [42] D. Zhang, B. Mei, H. Zhang, Q. Yang, and Y. Rao, *IEEE Trans. Magn.* **51**, 11 (2015).
- [43] Y. Hashimoto, S. Daimon, R. Iguchi, Y. Oikawa, K. Shen, K. Sato, D. Bossini, Y. Tabuchi, T. Satoh, B. Hillebrands, G. E. W. Bauer, T. H. Johansen, A. Kirilyuk, T. Rasing, and E. Saitoh, *Nat. Commun.* **8**, 15859 (2017).
- [44] S. Demokritov, B. Hillebrands, and A. N. Slavin, *Phys. Rep.* **348**, 441 (2001).
- [45] M. van Kampen, C. Jozsa, J. T. Kohlhepp, P. LeClair, L. Lagae, W. J. M. de Jonge, and B. Koopmans, *Phys. Rev. Lett.* **88**, 227201 (2002).
- [46] M. C. Onbasli, A. Kehlberger, D. H. Kim, G. Jakob, M. Klaui, A. V. Chumak, B. Hillebrands, and C. A. Ross, *APL Mater* **2**, 106102 (2014).
- [47] M. J. Hurben and C. E. Patton, *J. Appl. Phys.* **83**, 4344 (1998).
- [48] M. Kostylev, A. A. Stashkevich, A. O. Adeyeye, C. Shakespeare, N. Kostylev, N. Ross, K. Kennewell, R. Magaraggia, Y. Roussigné, and R. L. Stamps, *J. Appl. Phys.* **108**, 103914 (2010).
- [49] B. M. Howe, S. Emori, H. M. Jeon, T. M. Oxholm, J. G. Jones, K. Mahalingam, Y. Zhuang, N. X. Sun, and G. J. Brown, *IEEE Magn. Lett.* **6**, 1 (2015).
- [50] Y. H. Rao, D. N. Zhang, L. C. Jin, Z. Y. Zhong, Q. H. Yang, M. M. Li, J. Li, Y. Yang, G. Wang, G. W. Gan, and H. W. Zhang, *J. Magn. Magn. Mater.* **490**, 165442 (2019).
- [51] C. Liu, S. Wu, J. Zhang, J. Chen, J. Ding, J. Ma, Y. Zhang, Y. Sun, S. Tu, H. Wang, P. Liu, C. Li, Y. Jiang, P. Gao, D. Yu, J. Xiao, R. Duine, M. Wu, C. W. Nan, J. Zhang, and H. Yu, *Nat. Nanotechnol.* **14**, 691 (2019).
- [52] A. Prabhakar and D. D. Stancil, *Spin Waves* (Springer, New York, 2009).
- [53] Y. V. Gulyaev, P. Zilberman, G. Kazakov, B. Nam, V. Tikhonov, Y. A. Filimonov, and A. Khe, *Sov. Phys. JETP* **34**, 477 (1981).
- [54] N. Vukadinovic and J. B. Youssef, *Phys. Rev. B* **100**, 224423 (2019).
- [55] E. R. Rosenberg, L. Beran, C. O. Avci, C. Zeledon, B. Q. Song, C. Gonzalez-Fuentes, J. Mendil, P. Gambardella, M. Veis, C. Garcia, G. S. D. Beach, and C. A. Ross, *Phys. Rev. Mater.* **2**, 094405 (2018).
- [56] C. N. Wu, C. C. Tseng, Y. T. Fanchiang, C. K. Cheng, K. Y. Lin, S. L. Yeh, S. R. Yang, C. T. Wu, T. Liu, M. Wu, M. Hong, and J. Kwo, *Sci. Rep.* **8**, 11087 (2018).
- [57] J.-M. Beaujour, D. Ravelosona, I. Tudosa, E. E. Fullerton, and A. D. Kent, *Phys. Rev. B* **80**, 180415(R) (2009).
- [58] L. Flacke, L. Liensberger, M. Althammer, H. Huebl, S. Geprags, K. Schultheiss, A. Buzdakov, T. Hula, H. Schultheiss, E. R. J. Edwards, H. T. Nembach, J. M. Shaw, R. Gross, and M. Weiler, *Appl. Phys. Lett.* **115**, 122402 (2019).
- [59] D. M. Lattery, D. Zhang, J. Zhu, X. Hang, J. P. Wang, and X. Wang, *Sci. Rep.* **8**, 13395 (2018).